Stability and natural frequency of nonspherical mode of an encapsulated microbubble in a viscous liquid

Liu, YQ; Wang, Qian

DOI:
10.1063/1.4952583

Stability and natural frequency of nonspherical mode of an encapsulated microbubble in a viscous liquid

Yunqiao Liu, and Qianxi Wang

Citation: Physics of Fluids **28**, 062102 (2016); doi: 10.1063/1.4952583
View online: http://dx.doi.org/10.1063/1.4952583
View Table of Contents: http://aip.scitation.org/toc/phf/28/6
Published by the American Institute of Physics

PHYSICS OF FLUIDS **28**, 062102 (2016)

Stability and natural frequency of nonspherical mode of an encapsulated microbubble in a viscous liquid

Yunqiao Liu[1] and Qianxi Wang[2]
[1]*MOE Key Laboratory of Hydrodynamics, Department of Engineering Mechanics, Shanghai Jiao Tong University, Shanghai 200240, China*
[2]*School of Mathematics, University of Birmingham, Birmingham B15 2TT, United Kingdom*

(Received 25 November 2015; accepted 4 May 2016; published online 2 June 2016)

The dynamics of encapsulated microbubbles (EMBs) subject to an ultrasound wave have wide and important medical applications, including sonography, drug delivery, and sonoporation. The nonspherical shape oscillation of an EMB, termed as shape modes, is one of the core mechanisms of these applications and therefore its natural frequency is a fundamentally important parameter. Based on the linear stability theory, we show that shape modes of an EMB in a viscous Newtonian liquid are stable. We derive an explicit expression for the natural frequency of shape modes, in terms of the equilibrium radius of an EMB, and the parameters of the external liquid, coating, and internal gases. The expression is validated by comparing to the numerical results obtained from the dynamic equations of shape modes of an EMB. The natural frequency of shape modes shifts appreciably due to the viscosity of the liquid, and this trend increases with the mode number. The significant viscous effects are due to the no-slip condition for the liquid flow at the surface of an EMB. Our results show that when subject to an acoustic wave, the shape instability for an EMB is prone to appear if $2\omega_k/\omega_d = n$, where ω_k is the natural frequency of shape modes, ω_d is the driving frequency of the acoustic wave, and n is a natural number. The effects of viscosity on the natural frequency is thus critical in setting the driving frequency of ultrasound to avoid or activate shape modes of EMBs, which should be considered in the applications of medical ultrasound. *Published by AIP Publishing.* [http://dx.doi.org/10.1063/1.4952583]

I. INTRODUCTION

Dynamics of encapsulated microbubbles (EMBs) subject to ultrasound are associated with important applications in biomedicine, including sonography, drug/gene delivery, and sonoporation. Nonspherical stable shape oscillation of EMBs, termed as shape modes, is one of the core mechanisms of these medical applications. Microbubbles, used to enhance ultrasound contrast, were first reported by Gramiak and Shah.[1] Air bubbles introduced without a stabilizing shell were very short lived, and therefore a thin coating is used to stabilize the gas-liquid interface. After injection, EMBs can travel to all organs of the body within blood vessels. EMBs' high compressibility relative to blood/tissues leads to strong scattering of ultrasound waves, thereby enhancing blood-tissue contrast to improve the quality of image of blood vessels in sonography. Today, EMBs are used to enhance the reflectivity of perfused tissues in applications spanning cardiology and radiology.[2–4] For sonography, nonspherical shape modes give rise to frequency components—subharmonics, harmonics, and ultraharmonics—that are not at the incident ultrasound frequency, as can the spherical mode if driven to a nonlinear response.[5–8] These additional frequency components contribute to the signal scattered by EMBs and are important for distinguishing the microbubbles from the surrounding tissue, thus enhancing blood-tissue contrast.[6]

EMBs have been demonstrated as a new promising vehicle for targeted drug delivery to tumours or blood clots.[9–13] EMBs arrive at the site of tumours or blood clots in a few seconds after injection, and their lifetime is approximately 5 min.[14] When EMBs pass the focal region of ultrasound, they are activated by the ultrasound, leading to violent collapse and hence drugs/genes

release. The lack of tumour response to chemotherapy is well documented in many cancer types and is a major and life-limiting obstacle in cancer treatment. Collapsing MBs are believed to help to increase the permeability of cell membranes of nearby endothelial cells, facilitating targeted drug/gene delivery to the tumour neovasculature, a phenomenon known as sonoporation.[15–18] Nonspherical shape mode is one of the possible mechanisms for the breaking of the coating of EMBs for drug delivery, as well as sonoporation.[19,20] Therefore, it is important to determine the natural frequency of shape modes for an EMB, which is a critical parameter to avoid or to activate the nonspherical shape modes. Accordingly, this becomes the objective we endeavor to achieve in this work.

The natural frequency of shape modes for a gas bubble in an inviscid fluid is well known as given follows:[21]

$$\omega_k^{gas} = \sqrt{(k-1)(k+1)(k+2)\frac{\gamma}{\rho R_0^3}}, \tag{1.1}$$

where k is the order of shape mode, γ the surface tension, ρ the liquid density, and R_0 the equilibrium bubble radius. The inviscid model was improved by Prosperetti[22] by adding damping caused by a viscous vorticity field near the bubble wall. This was later simplified by assuming that the vorticity field occurs within a thin boundary layer near the bubble surface.[23–25] Alternatively, Shaw[26] modelled viscous damping effects for microbubble dynamics subject to ultrasound, using the Rayleigh dissipation function. The natural frequency of radial mode for a gas bubble in a viscoelastic medium was formulated by Gaudron *et al.*[27]

The existence of a thin coating for an EMB changes the natural frequency of radial oscillation and the intensity of the acoustic radiation.[28–30] The searching for the natural frequency of shape modes for an EMB is a current research topic. Tsiglifis and Pelekasis[31] obtained a square root dependence of the natural frequency of an EMB in terms of the bending stiffness of its coating. Their analysis is based on an inviscid flow model, where the tangential balance on the membrane is not satisfied. Liu *et al.*[32] derived the natural frequency of shape modes for an EMB in an inviscid liquid as follows:

$$\begin{aligned}\bar{\omega}_k^2 &= (k-1)(k+1)(k+2)\frac{\gamma}{\rho R_0^3} \\ &\quad + 2(k-1)(k+1)(k+2)\frac{G_s}{\rho R_0^3}\frac{(2k^2+2k-3)(k^2+k-1+\upsilon)G_b + 6G_sR_0^2}{(k^2+k-1+\upsilon)G_b + 2(2k^2+2k-1)G_sR_0^2},\end{aligned} \tag{1.2}$$

where G_s is the elastic modulus, G_b bending modulus, and υ Poisson ratio of the coating of the EMB.

In this paper, we will consider the shape stability and natural frequency ω_k of shape modes for an EMB in a viscous liquid, based on the following considerations. The viscous effects of the liquid and membrane detune the natural frequency significantly, which has been demonstrated for the spherical mode.[33] Liu *et al.*[32] showed that the dynamic equation of an EMB follows the structure of Mathieu's equation, like a gas bubble. This suggests that when subject to an acoustic wave, an EMB is most prone to be unstable under the following condition:[34]

$$2\omega_k/\omega_d = n, \tag{1.3}$$

where ω_k is the natural frequency of shape mode k, ω_d is the driving frequency of ultrasound, and n is a natural number. When $n = 1$, the condition of instability is $\omega_d = 2\omega_k$. However, the computational phase diagrams in Ref. 32 showed that the instability for an EMB subject to an acoustic wave is prone to appear when $\omega_d \approx 1.5\ \bar{\omega}_k$. This inconsistency implies that $\bar{\omega}_k$ calculated by the inviscid model (1.2) is significantly over-predicted.

The classical bubble dynamics are mainly inertial dominant, where the gas-liquid interface is assumed being shear-free.[35,36] But the liquid flow bears a no-slip condition on the membrane of an EMB, where the liquid moves with the deforming membrane, generating vorticity near the interface. We model the effects of viscosity of the surrounding liquid to an EMB following the work of Prosperetti,[22] by solving the toroidal component of the vorticity field coupled with the basic

potential flow field. Loughran *et al.*[37] carried out numerical analysis for the shape modes of an EMB in a viscous liquid, using Prosperetti's theory.[22] Our developments versus theirs are that we perform analytical stability analysis for the phenomenon and obtain analytical expression for the natural frequency of shape modes.

The membrane of an EMB is usually composed of albumin, galactose, lipid, or polymers,[38] which can be studied based on continuum mechanics.[39–46] In order to bypass the complexity of multiscale coupling, we adopt a viscoelastic model to describe the mechanics of the membrane. The fluid flow and membrane deformation are coupled by assuming that the velocity and stress are continuous both normally and tangentially on the membrane.

The remaining paper is organized as follows. In Sec. II, dynamic equations for shape modes of an EMB is briefed, the stability of the shape mode is studied, and the natural frequency of the shape mode is obtained analytically. The ranges of parameters for EMBs applied in medical ultrasound are discussed in Sec. III A. The natural frequency obtained is validated by comparing with the numerical results in Sec. III B. Our computations in Sec. III C show that an EMB resonates when the driving frequency ω_d of an acoustic wave is twice of the natural frequencies ω_k of shape modes considering viscous effects, i.e., $\omega_d = 2\omega_k$. The variations of the natural frequency of an EMB are analyzed in terms of the membrane parameters and liquid viscosity in Sec. III D. Viscous effects are analyzed in terms of the toroidal distribution of vorticity in Sec. III E. The summary and conclusions are given in Sec. IV.

II. PROBLEM FORMULATION

A. Dynamic equations for shape modes of an EMB

Consider a gas-filled microbubble encapsulated in a membrane, suspended in an unbounded incompressible Newtonian liquid, and subject to an acoustic wave, as shown in Fig. 1. A Cartesian coordinate system O-xyz and a spherical coordinate system (r, θ, ϕ) are adopted with the origin at the centre of the initial spherical encapsulated microbubble (EMB) and the z-axis along the wave direction. The acoustic pressure at the location of the bubble is characterized by dimensionless amplitude ε and a driving frequency ω_d,

$$p_\infty = p_0 [1 + \varepsilon \sin(\omega_d t)], \tag{2.1}$$

where p_0 is the ambient pressure. Here we assume that the wavelength of the acoustic wave is large compared to the bubble size. The physical and mathematical formulations for the dynamics of an EMB are following the work of Liu *et al.*,[32] which are briefly described as follows for completeness.

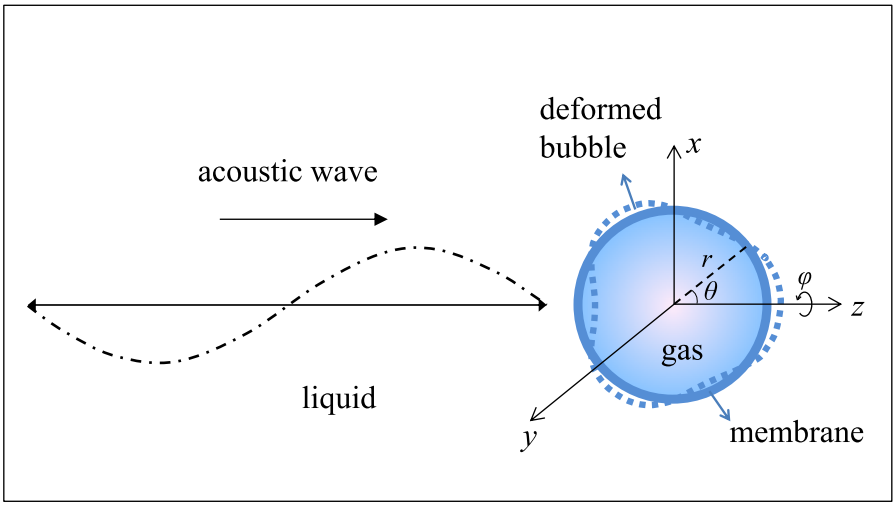

FIG. 1. The configuration and coordinate systems for a gas-filled microbubble encapsulated in a membrane, suspended in an unbounded incompressible Newtonian liquid, and subject to an acoustic wave.

The system consists of the external liquid, membrane, and internal gases of the EMB. The governing equations for the external flow to the EMB are the continuity equation and the Navier-Stokes equation,

$$\nabla \cdot \mathbf{u} = 0, \tag{2.2a}$$

$$\rho \frac{\partial \mathbf{u}}{\partial t} + \rho(\mathbf{u} \cdot \nabla)\mathbf{u} = -\nabla p + \mu_l \nabla \cdot (\nabla \mathbf{u} + \nabla \mathbf{u}^{\mathrm{T}}), \tag{2.2b}$$

where $\mathbf{u}$ denotes the velocity of the liquid flow, and p, ρ, and μ_l are the pressure, density, and viscosity of the liquid. The liquid velocity satisfies the no-slip condition on the membrane of an EMB.

It is assumed that the pressure of the gases within an EMB is uniform and the shear stress on the membrane of an EMB due to the interior gases is negligible, since the density and viscosity of the internal gases are small compared to those of the external liquid. The expansion and contraction of the internal gases are assumed to be adiabatic, with the internal pressure p_g being given as follows:

$$p_g = p_{g0}\left(\frac{V_0}{V}\right)^{\Gamma}, \tag{2.3}$$

where V_0 and V are the initial and transient volume of the EMB, p_{g0} is the initial pressure, and Γ is the polytropic index of the interior gases.

The membrane is subject to the liquid stress $\mathbf{n} \cdot \left(-p\mathbf{I} + 2\mu_l \left(\nabla \mathbf{u} + \nabla \mathbf{u}^{\mathrm{T}}\right)\right)$ and the gas pressure load $p_g \mathbf{n}$, where $\mathbf{n}$ is the unit normal vector on the surface pointing to the liquid and $\mathbf{I}$ is the unit tensor. The dynamic equation of the membrane thus states

$$\mathbf{n} \cdot \left(-p\mathbf{I} + 2\mu_l \left(\nabla \mathbf{u} + \nabla \mathbf{u}^{\mathrm{T}}\right)\right) + p_g \mathbf{n} - (\gamma \nabla \cdot \mathbf{n})\mathbf{n} = \mathbf{F}, \tag{2.4}$$

where γ is surface tension, and the term containing γ is kept to make this model suitable for a gas bubble too by setting $\mathbf{F} = 0$. For an EMB, the surface tension becomes zero because the membrane separates the liquid-gas interface. The hydrodynamic traction across the membrane is balanced by the stress $\mathbf{F}$ exerted on the membrane by itself, which is given by the surface divergence of the elastic tension tensor,[47]

$$\mathbf{F} = -(\mathbf{P} \cdot \nabla) \cdot (\boldsymbol{\tau} + \mathbf{qn}), \tag{2.5}$$

where $\mathbf{P} = \mathbf{I} - \mathbf{nn}$ is the tangential projection operator, $\boldsymbol{\tau}$ the in-plane stress, and $\mathbf{q}$ the transverse shear tension, which is expressed in terms of bending moment $\mathbf{m}$ as $\mathbf{q} = [(\mathbf{P} \cdot \nabla) \cdot \mathbf{m}] \cdot \mathbf{P}$. We employ the neo-Hookean law[48] for the in-plane stress, the linear law for the membrane viscosity, and the Love law[49] for the bending moment. The expression of the membrane stress is referred to Ref. 32.

The surface perturbation to a spherical EMB can be expanded in terms of the spherical harmonics,[50–52] in the spherical coordinate (r, θ, ϕ). Since the deformation of an EMB in the azimuthal direction ϕ is at the higher order,[53] we restrict our attention to an axisymmetric system, not considering the azimuthal mode. The axisymmetric deformation of the membrane in the radial and zenith directions, (r_s, Θ_s), is thus given as follows in terms of the Legendre polynomials $P_k(\cos\theta)$ and $P_k^1(\cos\theta) = dP_k(\cos\theta)/d\theta$, respectively:

$$r_s(\theta, t) = R(t) + \sum_{k=2}^{\infty} a_k(t) P_k(\cos\theta), \tag{2.6a}$$

$$\Theta_s(\theta, t) = \theta + \frac{1}{R(t)} \sum_{k=2}^{\infty} b_k(t) P_k^1(\cos\theta), \tag{2.6b}$$

assuming a_k, $b_k \ll R(t)$. The summation of order of shape modes is for $k \geq 2$, since $k = 1$ is associated with the translation of an EMB without deformation, which is not considered in this work.

To investigate the viscous effects of the liquid, we decompose the velocity into a potential part $\mathbf{u}_p$ and a viscous correction $\mathbf{u}_v$, following the work of Prosperetti.[22] The potential part is solved

using Laplace's equation and the normal velocity distribution on the EMB surface,[54] while the viscous correction is solved using the vorticity form of the linearized Navier-Stokes equation.[22] The vorticity of the flow is further decomposed into the poloidal $P(r,t)$ and toroidal $T(r,t)$ components as follows:

$$\nabla \times \mathbf{u}_v = \sum_{k=2}^{\infty} \left[\nabla \times \nabla \times (P(r,t)P_k(\cos\theta)\mathbf{e}_r) + \nabla \times T(r,t)P_k(\cos\theta)\mathbf{e}_r\right]. \tag{2.7}$$

Due to axisymmetry, the poloidal component $P(r,t)$ does not change in the azimuth direction, and only the toroidal component $T(r,t)$ contributes to the vorticity dissipation, which satisfies[22]

$$\rho\frac{\partial T}{\partial t} + \rho\frac{\partial}{\partial r}\left[\dot{R}(R/r)^2 T\right] - \mu_l\frac{\partial^2 T}{\partial r^2} + \mu_l k(k+1)\frac{T}{r^2} = 0. \tag{2.8}$$

The dynamic equations for an EMB are then obtained by Liu *et al.*,[32] by expanding (2.4) in terms of perturbation series, and making use of the orthogonality of the Legendre polynomials. Their model consists of the radial oscillation equation and the dynamic equations for shape modes in the normal and tangential directions as follows.

The radial oscillation equation of an EMB is

$$R\ddot{R} + \frac{3}{2}\dot{R}^2 + \frac{1}{\rho}\left[\frac{2\gamma}{R} + 4\mu_l\frac{\dot{R}}{R} - p_{g0}\left(\frac{R_0}{R}\right)^{3\Gamma} + p_\infty + \frac{2G_s(R^6 - R_0^6)}{R^7} + 4\mu_s\frac{\dot{R}}{R^2}\right] = 0, \tag{2.9}$$

where R_0 is the initial bubble radius when the bubble is assumed being in equilibrium, G_s and μ_s are the elastic modulus and viscosity of the membrane, the over dot denotes the derivative with respect to time t, and p_∞ is the acoustic pressure. Linearizing this equation, one can obtain the zeroth-order (spherical mode) natural frequency for an EMB in a Newtonian fluid,[32]

$$\omega_0 = \sqrt{\frac{3\Gamma p_0}{\rho R_0^2} + \frac{(6\Gamma - 2)\gamma}{\rho R_0^3} + \frac{12G_s}{\rho R_0^3}}, \tag{2.10}$$

where p_0 is the ambient pressure.

The shape oscillation equation for mode $k \geq 2$ of an EMB is

$$\begin{aligned}
&\frac{\rho R}{k+1}\ddot{a}_k + \left[\frac{3\rho}{k+1}\dot{R} + \frac{2(k+2)\mu_l}{R}\right]\dot{a}_k + \left[-\frac{k-1}{k+1}\rho\ddot{R} + \frac{(k+2)(k-1)\gamma}{R^2} + \frac{4(k-1)\mu_l\dot{R}}{R^2}\right]a_k \\
&\quad + k\mu_l\frac{T(R,t)}{R} + k\rho\frac{\dot{R}}{R}\int_R^\infty\left[\left(\frac{R}{s}\right)^3 - 1\right]\left(\frac{R}{s}\right)^k T(s,t)ds \\
&\quad - 2k(k+1)\mu_l R^{k-2}\int_R^\infty s^{-k}T(s,t)ds \\
&\quad = \frac{G_s}{R^8}[2(R^6 - 7R_0^6)a_k + 6k(k+1)R_0^6 b_k] - \frac{G_b}{R^4}[k(k+1)(k^2+k-1+\upsilon)(a_k - b_k)] \\
&\quad\quad - \frac{2\mu_s}{R^3}[-4a_k\dot{R} + 2R\dot{a}_k + k(k+1)(\dot{R}b_k - R\dot{b}_k)],
\end{aligned} \tag{2.11}$$

where G_b is the bending modulus of the membrane and υ is the Poisson ration.

The tangential dynamic equation for mode $k \geq 2$ of an EMB is

$$\begin{aligned}
&\mu_l\left[(2k+4)\frac{\dot{a}_k}{R} - (2k-2)\frac{a_k\dot{R}}{R^2} - (k+1)\frac{T(R,t)}{R} - 2(k+1)R^{k-2}\int_R^\infty s^{-k}T(s,t)ds\right] \\
&\quad = \frac{G_s(k+1)}{R^8}\left((R^6 - 7R_0^6)a_k + \left(3k(k+1)R_0^6 + (k-1)(k+2)R^6\right)b_k\right) \\
&\quad\quad - \frac{G_b}{R^4}(k+1)(k^2+k-1+\upsilon)(a_k - b_k) \\
&\quad\quad + \frac{2\mu_s(k+1)}{R^3}\left(2a_k\dot{R} - R\dot{a}_k + (k^2+k-1)(R\dot{b}_k - \dot{R}b_k)\right).
\end{aligned} \tag{2.12}$$

Eqs. (2.11) and (2.12) describe the dynamics of the kth shape mode of an EMB. The right hand sides of (2.11) and (2.12) are the membrane stress resulting from deformation. The amplitudes in the radial and zenith directions a_k and b_k are coupled, so does the deformation of the membrane in two directions. The toroidal component of vorticity is embodied in the integral terms in the equations.

The no-slip condition at the surface of an EMB implies $u_\theta = r_s(\theta,t)\frac{\partial \Theta_s(\theta,t)}{\partial t}$. Substituting (2.6) yields[32]

$$\dot{b}_k - \frac{\dot{R}}{R}b_k = -\frac{1}{k+1}\left(\dot{a}_k + \frac{2a_k\dot{R}}{R}\right) + R^{k-1}\int_R^\infty s^{-k}T(s,t)ds. \tag{2.13}$$

Equations (2.9), (2.11), and (2.13) are solved numerically for the unknowns functions $R(t)$, $a_k(t)$, and $b_k(t)$, by using the fourth-order Runge-Kutta method, in which the integrals in (2.11) and (2.13) are calculated numerically by using the composite trapezoidal rule. The toroidal field $T(r,t)$ is updated at every time step, by solving Equation (2.8) using the second-order finite difference method, with the boundary condition $T(R,t)$ at the surface of an EMB obtained from (2.12) and the far field condition $T \to 0$ at infinity.

B. Stability analysis and natural frequency of shape mode

In the flow modelling described in Sec. II A, we assumed that the flow is irrotational in a bulk volume and the viscosity of the flow is only appreciable in a thin boundary layer near an EMB surface. This assumption is only suitable for the cases with a large Reynolds number Re. Some of medical applications of EMBs coupled with ultrasound are associated large Reynolds numbers. In fact, $Re = \rho R_0^2\omega_M/\mu_l$, where ω_M is the larger of the natural frequency ω_0 of an EMB and driving wave frequency ω_d. The Reynolds number is estimated in the range of Re = 75–1170 for the typical values of the parameters for the phenomenon: $p_0 = 1\times10^5$ Pa, $\rho = 10^3$ kg m^{-3}, $\mu_l = 1\times10^{-3}$ kg (m s)$^{-1}$, $\Gamma = 1.4$, R_0 = 3–20 μm, and G_s = 0.05–5 N m^{-1}.

The thickness of the boundary layer is estimated as $O\left(R_0/\sqrt{Re}\right) = O\left(\sqrt{\mu_l/(\rho\omega_M)}\right)$,[22,37,55] which is given as follows with a cutoff:[56]

$$\chi = \min\left(\sqrt{\frac{\mu_l}{\rho\omega_M}}, \frac{R_0}{2k}\right). \tag{2.14}$$

To perform analytical analyses, the integrals in (2.11)–(2.13) are approximated by the products of the integrands evaluated at the bubble surface and the thickness of the boundary layer, i.e.,

$$\int_R^\infty \left[\left(\frac{R}{s}\right)^3 - 1\right]\left(\frac{R}{s}\right)^k T(s,t)ds \approx 0, \tag{2.15a}$$

$$\int_R^\infty s^{-k}T(s,t)ds \approx R^{-k}T(R,t)\chi. \tag{2.15b}$$

Substituting (2.14) and (2.15) into (2.11) and (2.12), we have the dynamic equations for the kth order shape mode in the normal and tangential directions, respectively, as follows:

$$\ddot{a}_k + C_{a1}\dot{a}_k + C_{b1}\dot{b}_k + C_a a_k + C_b b_k = 0, \tag{2.16a}$$

$$D_{a1}\dot{a}_k + D_{b1}\dot{b}_k + D_a a_k + D_b b_k = 0, \tag{2.16b}$$

where the coefficients are

$$C_{a1} = \left[-2(k+2)(k^2-1) + \frac{k(k+2)R_0}{\chi}\right]\frac{\mu_l}{\rho R_0^2} - (k-1)(k+1)(k+2)\frac{2\mu_s}{\rho R_0^3}, \tag{2.17a}$$

$$C_{b1} = k(k+1)(k+2)\frac{\mu_l}{\rho\chi R_0} + k(k-1)(k+1)^2(k+2)\frac{2\mu_s}{\rho R_0^3}, \tag{2.17b}$$

$$C_a = (k-1)(k+1)(k+2)\frac{\gamma + G_s}{\rho R_0^3}, \tag{2.17c}$$

$$C_b = 4k(k-1)(k+1)^2(k+2)\frac{G_s}{\rho R_0^3}, \tag{2.17d}$$

$$D_{a1} = \left[-\frac{1}{\chi} + \frac{2(k+1)}{R_0}\right]\mu_l + \frac{2(k+1)}{R_0^2}\mu_s, \tag{2.17e}$$

$$D_{b1} = -(k+1)\left(\frac{1}{\chi} + \frac{2}{R_0}\right)\mu_l - (k+1)(k^2+k-1)\frac{2\mu_s}{R_0^2}, \tag{2.17f}$$

$$D_a = 6(k+1)\frac{G_s}{R_0^2} + (k+1)(k^2+k-1+\upsilon)\frac{G_b}{R_0^4}, \tag{2.17g}$$

$$D_b = -(k+1)(2k^2+2k-1)\frac{2G_s}{R_0^2} - (k+1)(k^2+k-1+\upsilon)\frac{G_b}{R_0^4}. \tag{2.17h}$$

For the purpose of linear analysis, the transient bubble radius $R(t)$ is replaced by R_0 in (2.17). Note that the terms in (2.17) associated with the viscosities of the liquid and membrane were neglected in the work of Liu *et al.*,[32] i.e., they assumed $C_{a1} = C_{b1} = D_{a1} = D_{b1} = 0$ in deriving the natural frequency of shape modes of an EMB. But the viscous effects of the liquid and membrane are considered in this work. Our computations in Sec. III show clearly that the viscous effects are essential and not negligible.

The dimensionless form of (2.16) can be written as follows:

$$\ddot{\bar{a}}_k + \bar{c}_{a1}\dot{\bar{a}}_k + \bar{c}_{b1}\dot{\bar{b}}_k + \bar{c}_a\bar{a}_k + \bar{c}_b\bar{b}_k = 0, \tag{2.18a}$$

$$\overline{d}_{a1}\dot{\bar{a}}_k + \overline{d}_{b1}\dot{\bar{b}}_k + \overline{d}_a\bar{a}_k + \overline{d}_b\bar{b}_k = 0, \tag{2.18b}$$

where

$$\begin{gathered}
\bar{t} = \omega_k t, \qquad \bar{a}_k = a_k/R_0, \qquad \bar{b}_k = b_k/R_0, \\
\bar{c}_{a1} = \frac{C_{a1}}{\omega_k}, \quad \bar{c}_{b1} = \frac{C_{a1}}{\omega_k}, \qquad \bar{c}_a = \frac{C_a}{\omega_k^2}, \qquad \bar{c}_b = \frac{C_b}{\omega_k^2}, \\
\overline{d}_{a1} = \frac{D_{a1}}{\omega_k}, \quad \overline{d}_{b1} = \frac{D_{a1}}{\omega_k}, \qquad \overline{d}_a = \frac{D_a}{\omega_k^2}, \qquad \overline{d}_b = \frac{D_b}{\omega_k^2}.
\end{gathered} \tag{2.19}$$

To simplify (2.18a) and (2.18b), we perform the following order analysis using (2.14), (2.17), and (2.19):

$$O(\bar{c}_{a1}) = O(\bar{c}_{b1}) = \frac{1}{\rho R_0\omega_k} O\left(\sqrt{\rho\omega_0\mu_l}, \frac{\mu_s}{R_0^2}\right), \tag{2.20a}$$

$$O(\bar{c}_a) = O(\bar{c}_b) = \frac{1}{\rho R_0\omega_k^2}\frac{G_s}{R_0^2}, \tag{2.20b}$$

$$O\left(\overline{d}_{a1}\right) = O\left(\overline{d}_{b1}\right) = \frac{1}{\omega_k} O\left(\sqrt{\rho\omega_0\mu_l}, \frac{\mu_s}{R_0^2}\right), \tag{2.20c}$$

$$O\left(\overline{d}_a\right) = O\left(\overline{d}_b\right) = \frac{1}{\omega_k^2} O\left(\frac{G_s}{R_0^2}, \frac{G_b}{R_0^4}\right). \tag{2.20d}$$

For medical ultrasonic applications of EMBs, the ranges of the parameter to be discussed in Sec. III A are $R_0 = O(1)$ μm, $\mu_l = O(10^{-3})$ kg (m s)$^{-1}$, $G_s \le O(1)$ N m^{-1}, $G_b \le O(10^{-12})$ N m, $\mu_s \le O(10^{-8})$ kg s^{-1}, and $O(\omega_0) = O(\omega_k) = O(10^6)$ s^{-1}. The following estimations can be made using (2.20) and the range of parameters: $O\left(\frac{\bar{c}_{a1}}{\bar{c}_a}\right) = O\left(\frac{\bar{c}_{b1}}{\bar{c}_b}\right) \le O\left(10^{-2}\right)$ and $O\left(\frac{\overline{d}_{a1}}{\overline{d}_a}\right) = O\left(\frac{\overline{d}_{b1}}{\overline{d}_b}\right) = O\left(10^{-2}\right)$. We express $(\bar{c}_{a1}, \bar{c}_{b1}) = \delta\left(\overline{C}_{a1}, \overline{C}_{b1}\right)$ and $\left(\overline{d}_{a1}, \overline{d}_{b1}\right) = \delta\left(\overline{D}_{a1}, \overline{D}_{b1}\right)$, where $0 < \delta = O(10^{-2}) \ll 1$, $\overline{C}_{a1}, \overline{C}_{b1}$ are comparable with $\bar{c}_a, \bar{c}_b$, and $\overline{D}_{a1}, \overline{D}_{b1}$ are comparable with $\overline{d}_a, \overline{d}_b$. We thus have

$$\ddot{\bar{a}}_k + \delta\left(\overline{C}_{a1}\dot{\bar{a}}_k + \overline{C}_{b1}\dot{\bar{b}}_k\right) + \bar{c}_a\bar{a}_k + \bar{c}_b\bar{b}_k = 0, \tag{2.21a}$$

$$\delta\left(\overline{D}_{a1}\dot{\bar{a}}_k + \overline{D}_{b1}\dot{\bar{b}}_k\right) + \overline{d}_a\bar{a}_k + \overline{d}_b\bar{b}_k = 0. \tag{2.21b}$$

Using (2.21b), we have

$$\bar{b}_k = -\frac{\bar{d}_a}{\bar{d}_b}\bar{a}_k - \frac{\delta}{\bar{d}_b}\left(\bar{D}_{a1}\dot{\bar{a}}_k + \bar{D}_{b1}\dot{\bar{b}}_k\right). \tag{2.22a}$$

Therefore, we have $\bar{b}_k = -\frac{\bar{d}_a}{\bar{d}_b}\bar{a}_k + O(\delta)$ and $\dot{\bar{b}}_k = -\frac{\bar{d}_a}{\bar{d}_b}\dot{\bar{a}}_k + O(\delta)$. Substituting this into Eq. (2.22a), we have

$$\begin{aligned}\bar{b}_k &= -\frac{\bar{d}_a}{\bar{d}_b}\bar{a}_k - \frac{\delta}{\bar{d}_b}\left(\bar{D}_{a1}\dot{\bar{a}}_k + \bar{D}_{b1}\left(-\frac{\bar{d}_a}{\bar{d}_b}\dot{\bar{a}}_k + O(\delta)\right)\right)\\ &= -\frac{\bar{d}_a}{\bar{d}_b}\bar{a}_k - \frac{\delta}{\bar{d}_b}\left(\bar{D}_{a1} - \bar{D}_{b1}\frac{\bar{d}_a}{\bar{d}_b}\right)\dot{\bar{a}}_k + O(\delta^2).\end{aligned} \tag{2.22b}$$

We then substitute (2.22b) into (2.21a), keeping the first two orders in δ, and obtain

$$\ddot{\bar{a}}_k + \left(\bar{c}_{a1} - \bar{c}_{b1}\frac{\bar{d}_a}{\bar{d}_b} - \frac{1}{\bar{d}_b}\left(\bar{d}_{a1} - \bar{d}_{b1}\frac{\bar{d}_a}{\bar{d}_b}\right)\right)\dot{\bar{a}}_k + \left(\bar{c}_a - \bar{c}_b\frac{\bar{d}_a}{\bar{d}_b}\right)\bar{a}_k + O(\delta^2) = 0. \tag{2.23}$$

Using (2.20), we make the following estimation for the ranges of the parameter considered:

$$\frac{O\left(\frac{1}{\bar{d}_b}\left(\bar{d}_{a1} - \bar{d}_{b1}\frac{\bar{d}_a}{\bar{d}_b}\right)\right)}{O\left(\bar{c}_{a1} - \bar{c}_{b1}\frac{\bar{d}_a}{\bar{d}_b}\right)} = \frac{O\left(\frac{\bar{d}_{a1}}{\bar{d}_b}\right)}{O(\bar{c}_{a1})} = O\left(\frac{\bar{d}_{a1}}{\bar{d}_b\bar{c}_{a1}}\right) = O\left(\frac{\rho R_0}{\bar{d}_b}\right) = O(10^{-3}). \tag{2.24}$$

Thus $O\left(\bar{c}_{a1} - \bar{c}_{b1}\frac{\bar{d}_a}{\bar{d}_b}\right) \gg O\left(\frac{1}{\bar{d}_b}\left(\bar{d}_{a1} - \bar{d}_{b1}\frac{\bar{d}_a}{\bar{d}_b}\right)\right)$. Equation (2.24) further becomes

$$\ddot{\bar{a}}_k + \left(\bar{c}_{a1} - \bar{c}_{b1}\frac{\bar{d}_a}{\bar{d}_b}\right)\dot{\bar{a}}_k + \left(\bar{c}_a - \bar{c}_b\frac{\bar{d}_a}{\bar{d}_b}\right)\bar{a}_k + O(\delta^2) = 0. \tag{2.25}$$

In the dimensional form, (2.25) becomes

$$\ddot{a}_k + \left(C_{a1} - C_{b1}\frac{D_a}{D_b}\right)\dot{a}_k + \left(D_a - D_b\frac{D_a}{D_b}\right)a_k = 0. \tag{2.26a}$$

Substituting (2.17) into (2.26a) yields

$$\ddot{a}_k + \Psi\dot{a}_k + \Phi a_k = 0, \tag{2.26b}$$

where

$$\begin{aligned}\Psi \;=\; & 2(k+2)\left(\frac{kR_0}{2\chi} - k^2 + 1\right)\frac{\mu_l}{\rho R_0^2} - 2(k-1)(k+1)(k+2)\frac{\mu_s}{\rho R_0^3}\\ & + k(k+1)(k+2)\frac{\left((k^2+k-1+\upsilon)G_b + 6G_sR_0^2\right)\left(R_0^2\mu_l + 2(k^2-1)\chi\mu_s\right)}{\rho R_0^3\chi\left((k^2+k-1+\upsilon)G_b + 2(2k^2+2k-1)G_sR_0^2\right)},\end{aligned} \tag{2.27a}$$

$$\Phi = (k-1)(k+1)(k+2)\frac{1}{\rho R_0^3}\left[\gamma + 2G_s\frac{(2k^2+2k-3)(k^2+k-1+\upsilon)G_b + 6G_sR_0^2}{(k^2+k-1+\upsilon)G_b + 2(2k^2+2k-1)G_sR_0^2}\right]. \tag{2.27b}$$

Supposing that a_k has the form of $a_k \sim e^{\sigma_k t}$, the characteristic equation of (2.26) is

$$\sigma_k^2 + \Psi\sigma_k + \Phi = 0. \tag{2.28}$$

Its solutions are

$$\sigma_k = -\frac{\Psi}{2} \pm \frac{\sqrt{\Delta}}{2}, \text{ where } \Delta = \Psi^2 - 4\Phi. \tag{2.29}$$

The damping coefficient Ψ is always non-negative (as shown in the Appendix). Ψ is equal to zero as $\mu_l = \mu_s = 0$ and $\Psi > 0$ as μ_l and/or μ_s are non-zero. We thus obtain the instability criterion of the phenomenon as follows. If $\Delta \geq 0$, we have $\sigma_k < 0$, and hence a_k and b_k decrease

monotonically. If $\Delta < 0$, a_k and b_k are oscillating functions with amplitudes decaying exponentially with time, $e^{-\Psi t/2}$. As such, shape modes of an EMB in a viscous liquid are always stable subject to small disturbance. As the viscosities of liquid and shell approach zero, the damping coefficient $\Psi \to 0$, the oscillation repeats for long time.

The imaginary part of σ_k is related to the natural frequency of an EMB in a viscous liquid: $\omega_k = Im(\sigma_k) = \sqrt{-\Delta}/2$ for $\Delta \le 0$, thus

$$\begin{aligned}\omega_k^2 =\ & (k-1)(k+1)(k+2)\frac{\gamma}{\rho R_0^3} \\ & + 2(k-1)(k+1)(k+2)\frac{G_s}{\rho R_0^3}\frac{(2k^2+2k-3)(k^2+k-1+\upsilon)G_b + 6G_sR_0^2}{(k^2+k-1+\upsilon)G_b + 2(2k^2+2k-1)G_sR_0^2} \\ & - \left[(k+2)\left(\frac{kR_0}{2\chi} - k^2 + 1\right)\frac{\mu_l}{\rho R_0^2} - (k-1)(k+1)(k+2)\frac{\mu_s}{\rho R_0^3}\right. \\ & \left. + k(k+1)(k+2)\frac{\left((k^2+k-1+\upsilon)G_b + 6G_sR_0^2\right)\left(R_0^2\mu_l + 2(k^2-1)\chi\mu_s\right)}{2\rho R_0^3\chi\left((k^2+k-1+\upsilon)G_b + 2(2k^2+2k-1)G_sR_0^2\right)}\right]^2.\end{aligned} \tag{2.30}$$

If the viscous effects are negligible, $\mu_l = \mu_s = 0$, ω_k is reduced to $\bar{\omega}_k$ given by (1.2), the undamped natural frequency of an EMB in an inviscid liquid. The term in (2.30) related to the viscosities of the liquid and membrane is always negative; therefore, the damped natural frequency ω_k with viscous effects predicted by (2.30) is always smaller than the undamped natural frequency $\bar{\omega}_k$ of (1.2). This is understandable since the viscosity inhibits the flow near the interface and the oscillation of the bubble, prolonging the oscillation period.

III. NUMERICAL ANALYSES

A. The ranges of the parameters

The bubble size is preferably large to increase efficacy in sonography,[60] but should be smaller than the blood capillary diameter for safety.[61] A lipid coated bubble is usually smaller than 5 μm in radius.[62] Most of polymer or albumin coated bubbles are smaller than 10 μm in radius.[31,58,63]

The viscosity of plasma is about 1.2 times that of water,[57] while the apparent viscosity of blood varies with the shear rate of velocity and hematocrits.[64] The apparent viscosity increases under low shear rate, e.g., in the center of a blood vessel, and decreases under high shear rate, e.g., near vessel walls. Besides, the apparent viscosity of blood increases with hematocrits, which depends on health conditions. The range of liquid viscosity is thus chosen as 0.5×10^{-3}–0.5×10^{-2} kg (m s)$^{-1}$.

A polymer bubble exhibits excellent stability because of its hard shell with G_s = 0.5–5 N m^{-1}.[59] Considering that a coating consisting of monolayer molecules is softer than that of polymer,[65] we choose the elastic modulus lower to 0.05 N m^{-1}. The bending modulus and membrane viscosity of EMBs have broad ranges 1×10^{-17}–1×10^{-12} N m[66] and 1×10^{-19}–1×10^{-8} kg s^{-1},[59] respectively. The effects of very small bending modulus and membrane viscosity are negligible, so that we choose the range of upper limits for these two parameters.

Accordingly, we choose the parameter ranges as shown in Table I.

TABLE I. The typical parameter ranges of the initial radius R_0, liquid viscosity μ_l, elastic modulus G_s, bending modulus G_b, and membrane viscosity μ_s of EMBs used in medical ultrasonics.

Parameters	Ranges of parameters
R_0	3–20 μm
μ_l	0.5×10^{-3}–0.5×10^{-2} kg (m s)$^{-1}$
G_s	0.05–5 N m^{-1}
G_b	1×10^{-14}–1×10^{-12} N m
μ_s	1×10^{-10}–1×10^{-8} kg s^{-1}

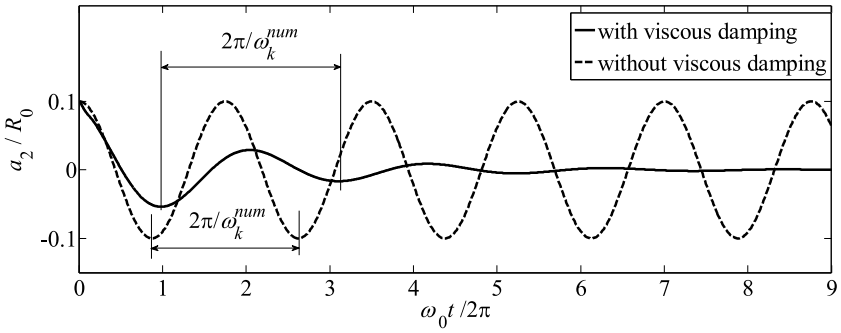

FIG. 2. Time history of shape mode 2 of an EMB for (a) $\rho = 10^3$ kg m^{-3}, $R_0 = 10$ μm, $\mu_l = 1\times10^{-3}$ kg (m s)$^{-1}$, $G_s = 0.5$ N m^{-1}, $G_b = 1\times10^{-13}$ N m, and $\mu_s = 1\times10^{-8}$ kg s^{-1}, and (b) $\mu_l = \mu_s = 0$, with the remaining parameters unchanged.

B. Evaluation of the analytical natural frequency of shape modes

If slightly disturbed and without any external driving force, an EMB undergoes shape mode oscillation at its natural frequency. The parameters for the first case are chosen as follows: $\rho = 10^3$ kg m^{-3}, $R_0 = 10$ μm, $\mu_l = 1\times10^{-3}$ kg (m s)$^{-1}$, $G_s = 0.5$ N m^{-1}, $G_b = 1\times10^{-13}$ N m, and $\mu_s = 1\times10^{-8}$ kg s^{-1}. We set initial disturbance as $a_2(0)/R_0 = 0.1$ for shape mode 2. The time history of a_2, obtained from (2.8) and (2.11)–(2.13) numerically, is shown in Fig. 2. For comparison, we also consider the case for $\mu_l = \mu_s = 0$, with the remaining parameters unchanged.

The bubble oscillates at constant amplitude without viscous effects but its amplitude is damped significantly with viscous effects. The time difference between two troughs of the oscillating curve provides the oscillation period and thus the corresponding natural frequency ω_k^{num} of the EMB. The oscillation period with viscous effects is larger than that without viscous effects, as shown in Fig. 2. This is consistent with the early observation to (2.30).

We then compare the natural frequencies of shape modes of EMBs of the analytical results ω_k obtained from (2.30) with numerical results ω_k^{num} from (2.8) and (2.11)–(2.13). Six cases are considered, and the parameters for case (a) are the same as in Fig. 2. For the rest five cases, only one parameter is changed with the remaining parameters being the same as the case (a): (b) $R_0 = 8$ μm, (c) $\mu_l = 5\times10^{-3}$ kg (m s)$^{-1}$, (d) $G_s = 1.0$ N m^{-1}, (e) $G_b = 1\times10^{-12}$ N m, and (f) $\mu_s = 1\times10^{-9}$ kg s^{-1}. The results for $\mu_l = \mu_s = 0$ are also displayed for every case, with the remaining parameters unchanged.

Table II shows the natural frequencies of shape modes $k = 2$, 3, 4 of EMBs for the cases ((a)–(f)). The undamped analytical natural frequency agrees well with that of the numerical results. The damped analytical natural frequency, in general, agrees with that of the numerical results. The small discrepancy for the latter should be due to the approximation associated with the boundary layer used in deriving expression (2.30). The natural frequency for the cases with viscous effects is obviously smaller than that without viscous effects and this trend increases with the mode number. In the case of spherical EMBs, viscosity only enters the analysis through the normal stress on the surface of the bubble but plays no role in the fluid body.[8,17] When an EMB undergoes nonspherical shape modes, the liquid material points at the coating move with it due to the no-slip boundary condition. A shear flow within a thin boundary layer nearby is thus generated by the tangential motion of the coating, whose variation amplitude increases with the shape mode.

For comparison, the corresponding results for a gas bubble at the same initial radius as case (a) are shown in the table, for which surface tension is chosen as $\gamma = 0.0729$ N m^{-1}. The natural frequency of shape modes for a gas bubble does not change significantly with the viscosity of liquid as an EMB does. This is attributed to the free-slip condition on the gas bubble surface.

C. Shape instability of an EMB subject to an acoustic wave

As noted in the introduction that shape instability for an EMB should be prone to appear, when the driving frequency of an acoustic wave is twice of the natural frequencies of shape modes,

TABLE II. Comparison of the natural frequencies of shape modes of EMBs of the analytical results ω_k and numerical results ω_k^{num} for (a) $R_0 = 10$ μm, $\mu_l = 1\times10^{-3}$ kg (m s)$^{-1}$, $G_s = 0.5$ N m^{-1}, $G_b = 1\times10^{-13}$ N m, $\mu_s = 1\times10^{-8}$ kg s^{-1}, (b) $R_0 = 8$ μm, (c) $\mu_l = 5\times10^{-3}$ kg (m s)$^{-1}$, (d) $G_s = 1.0$ N m^{-1}, (e) $G_b = 1\times10^{-12}$ N m, (f) $\mu_s = 1\times10^{-9}$ kg s^{-1}, and (g) gas bubble. For cases ((b)-(f)), only one parameter is changed with the remaining parameters being the same as the case (a). For the case (g), $\gamma = 0.0729$ N m^{-1} and the membrane parameters are taken as zero. The results for without damping are for $\mu_l = \mu_s = 0$, with the remaining parameters unchanged.

Case	k	$\bar{\omega}_k/2\pi$ (MHz) without damping	$\omega_k^{num}/2\pi$ (MHz) without damping	$\omega_k/2\pi$ (MHz) with damping	$\omega_k^{num}/2\pi$ (MHz) with damping
	2	0.29	0.29	0.25	0.24
a	3	0.38	0.38	0.32	0.32
	4	0.47	0.46	0.38	0.39
	2	0.41	0.41	0.35	0.33
b	3	0.54	0.54	0.44	0.45
	4	0.69	0.69	0.55	0.57
	2	0.29	0.29	0.16	0.18
c	3	0.38	0.38	0.27	0.24
	4	0.47	0.46	0.21	0.28
	2	0.41	0.41	0.38	0.35
d	3	0.52	0.53	0.47	0.45
	4	0.63	0.63	0.54	0.54
	2	0.31	0.31	0.28	0.26
e	3	0.49	0.49	0.44	0.42
	4	0.77	0.77	0.72	0.67
	2	0.29	0.29	0.26	0.24
f	3	0.38	0.38	0.34	0.32
	4	0.47	0.46	0.42	0.39
	2	0.14	0.15	0.15	0.14
g (gas bubble)	3	0.26	0.27	0.27	0.26
	4	0.40	0.40	0.41	0.41

i.e., $\omega_d = 2\omega_k$.[34] We want to see if it is true with the damped natural frequency obtained in this paper.

For the cases considered, we choose $p_0 = 1\times10^5$ Pa, $\varepsilon = 1$ for $k = 2$, 3, and $\varepsilon = 1.5$ for $k = 4$. The driving frequencies are set being twice of the undamped and damped natural frequencies of shape modes according to (1.2) or (2.30), respectively. The initial disturbance in shape modes is given as $a_k(0)/R_0 = 0.1$. The remaining parameters are kept the same as in Fig. 2 (for $\mu_l \neq 0$, $\mu_s \neq 0$). The developments of $a_k(t)$ are solved numerically from (2.8), (2.9), and (2.11)–(2.13).

For mode 2, we set $\omega_d = 2\pi\times0.58$, $2\pi\times0.5$ MHz, which are twice of the undamped and damped natural frequencies (see Table II, case a), i.e., $\omega_d = 2\bar{\omega}_k$, $2\omega_k$, respectively. Fig. 3(a) contrasts different time histories of $a_2(t)$ under the same driving amplitude but different frequencies. As $\omega_d = 2\bar{\omega}_k = 2\pi\times0.58$ MHz, the initial disturbance in the shape mode damps immediately and does not cause any instability. However, as $\omega_d = 2\omega_k = 2\pi\times0.5$ MHz, the initial disturbance in the shape mode develops rapidly and significantly with time, and the shape mode becomes obviously unstable.

For modes 3 and 4, we set the driving frequency of the incident wave at $\omega_d/2\pi = 0.76$, 0.64 MHz, and $\omega_d/2\pi = 0.94$, 0.76 MHz, respectively, which are twice of the undamped and damped natural frequencies (see Table II, case a, $k = 3$, 4), respectively. Similar features are observed as those in Fig. 3(a). The applied acoustic wave at the frequency being twice of the damped natural frequency generates shape instability rapidly and significantly, but that at the frequency being twice of the undamped natural frequency does not generate any instability (see Figs. 3(b) and 3(c)). As such, the shift of the natural frequency due to viscous effects is critical in setting the applied frequency of ultrasound to avoid or activate the shape modes of EMBs.

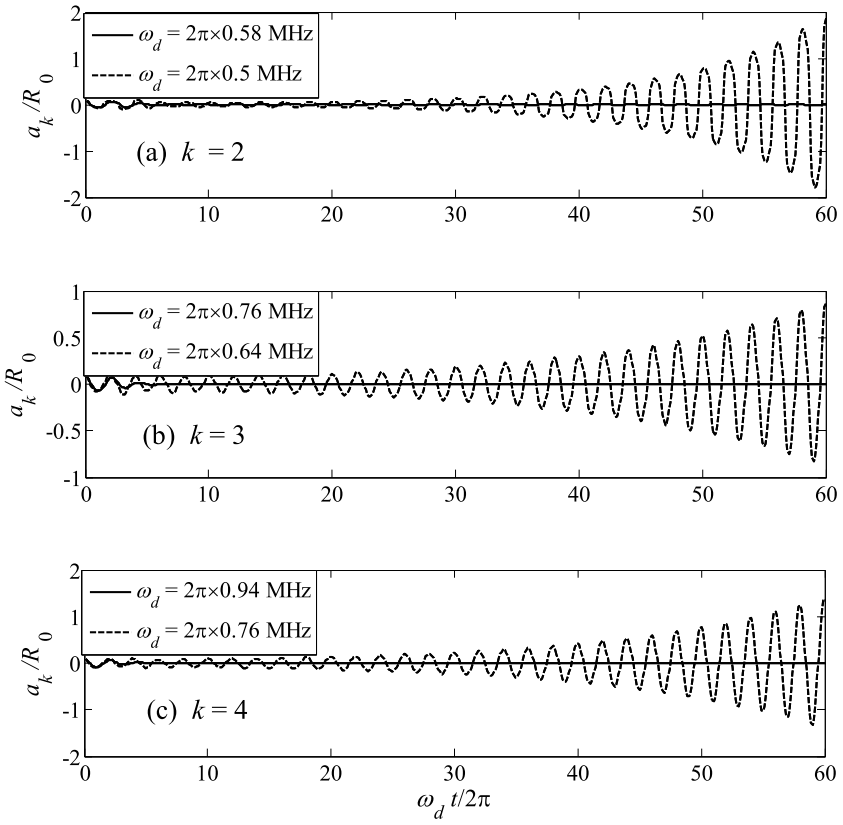

FIG. 3. Time developments of shape modes of an EMB subject to an acoustic wave with $p_0 = 1\times10^5$ Pa, for (a) $k = 2$, $\omega_d/2\pi = 0.58$, 0.5 MHz, $\varepsilon = 1$, (b) $k = 3$, $\omega_d/2\pi = 0.76$, 0.64 MHz, $\varepsilon = 1$, and (c) $k = 4$, $\omega_d/2\pi = 0.94$, 0.76 MHz, $\varepsilon = 1.5$. The remaining parameters are the same as in Fig. 1 for $\mu_l \neq 0$, $\mu_s \neq 0$.

When subject to an acoustic wave, an EMB undergoes damped oscillation due to viscosity if the wave amplitude is smaller than a threshold ε_{thr}, but becomes unstable if the amplitude is larger than ε_{thr}. Fig. 4 shows the stability diagram in terms of the threshold ε_{thr} of the amplitude versus the frequency $\omega_d/2\pi$ of the acoustic wave, for modes 2, 3, and 4 for the case (a) in Table II. We will analyze the critical driving frequency at which the threshold ε_{thr} reaches the minimum values, when an EMB is most prone to be unstable.

Recall that the natural frequencies for shape modes of the EMB for the case are $\omega_k/2\pi = 0.25$, 0.32, and 0.38 MHz for $k = 2$, 3, and 4, respectively (see Table II). For mode 2 (solid line), the minimum of ε_{thr} (occurring at the point M_{21} in the Fig. 4) is at $\omega_d = 2\pi\times0.48$ MHz, being approximately twice of $\omega_2 = 2\pi\times0.25$ MHz, i.e., $\omega_d \approx 2\omega_2$. And the secondary minimum M_{22} is at $\omega_d = 2\pi\times0.24$ MHz, being approximately equal to ω_2, i.e., $\omega_d \approx \omega_2$. For mode 4 (dashed line), the minimum (M_{41}) and the secondary minimum (M_{42}) occur at the driving frequencies $\omega_d = 2\pi\times0.41$ MHz and $2\pi\times0.22$ MHz, being approximately equal to ω_4 and $\omega_4/2$, respectively. The minimum of the curve for mode 3 (dotted line) is at $\omega_d = 2\pi\times0.48$ MHz, which should be attributed to the coupling effects between shape mode 3 and the radial resonance, since the natural frequency of the radial mode is $\omega_0/2\pi = 0.51$ MHz.

The computational results have shown that the damped natural frequency ω_k of (2.30) and the critical driving frequency ω_d, at which an EMB is most prone to be unstable, satisfy approximately the relationship $2\omega_k/\omega_d = n$, as predicted by Mathieu's equation.[34] The small discrepancy is expected, since the damped natural frequency ω_k is obtained based on the approximate linear theory. The undamped natural frequency of shape modes (1.2) does not satisfies the relationship $2\omega_k/\omega_d = n$.

While an EMB undergoes shape oscillation of mode k, the maximum deformation and stress should be associated with either the maximal value or the minimal value (negative) of a_k. Figs. 5(a),

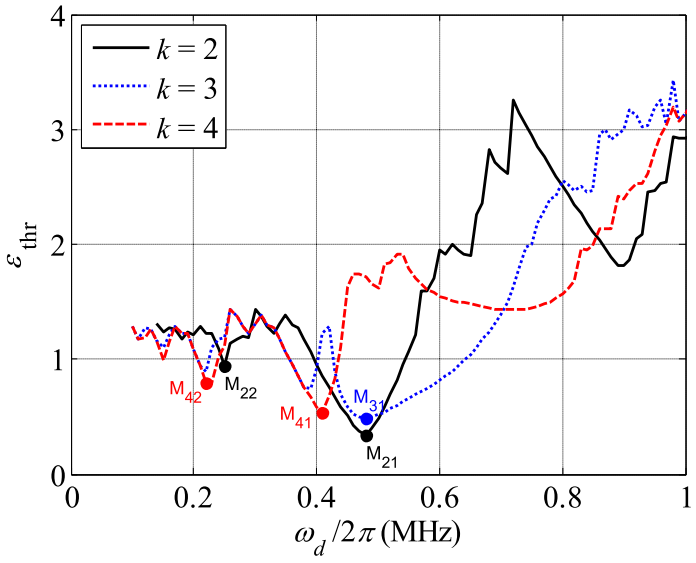

FIG. 4. Stability diagram in terms of the threshold ε_{thr} of the amplitude versus the frequency $\omega_d/2\pi$ of the acoustic wave, for modes 2, 3, and 4 for the case in Fig. 3.

5(b), and 5(c) show the shape of an EMB at the maximal and minimal values of a_k for shape modes $k = 2$, 3, and 4, for 40 cycles of oscillation, and the corresponding stress distribution, respectively. The driving force is set at the frequencies $\omega_d/2\pi = 0.5$, 0.64, 0.76 MHz, respectively, which are twice of the damped natural frequencies of the EMB (see Table II). The thick lines represent the bubble shape and the thin lines the distribution of stress. For the normal stress (left column of the figure), the inward or outward lines represent the direction of stress; for the tangential stress (right column), the inward lines represent compression and the outward lines represent extension. The maximal and minimal values of the normal and tangential stresses are denoted in the figures as well. The displacement and stress are periodical functions in the zenith angle θ with the periods π, $2\pi/3$, and $\pi/2$ for $k = 2$, 3, and 4, respectively. It is believed that the number of fragments of an EMB is determined by the dominant shape mode.[67] Correspondingly, we find from Fig. 5 (right column) that the maximal tangential stress, associated with the maximal extension, occurs at the centre of each concave part of the membrane, where the local radius of the EMB is at the minimum. At maximum of a_k, $\theta = \pi/2$, $3\pi/2$ for $k = 2$, $\theta = \pi/3$, π, $5\pi/3$ for $k = 3$, and $\theta = \pi/4$, $3\pi/4$, $5\pi/4$, $7\pi/4$, for $k = 4$, respectively. At minimum of a_k, $\theta = 0$, π for $k = 2$, $\theta = 0$, $2\pi/3$, $4\pi/3$ for $k = 3$, and $\theta = 0$, $\pi/2$, π, $3\pi/2$, for $k = 4$, respectively. These locations are weak spots, where the membrane is most prone to break.

D. Parameter studies of natural frequency of shape modes

We now investigate the damped natural frequency ω_k of shape modes of an EMB in terms of the equilibrium radius R_0, viscosity of liquid μ_l, elastic modulus G_s, bending modulus G_b, and membrane viscosity μ_s. Fig. 6 plots the natural frequency versus the above parameters for shape modes $k = 2$, 3, and 4, respectively, according to (2.30). In general, the natural frequency ω_k increases with the mode number k. As the equilibrium radius R_0 decreases, the natural frequency ω_k increases and so does the rate of increase (Fig. 6(a)). Among the membrane properties (Figs. 6(c)-6(d)), the natural frequency increases with the elastic modulus G_s and the bending modulus G_b, but decreases with the membrane viscosity μ_s. The elastic modulus plays a more important role in the natural frequency than the bending modulus and membrane viscosity. The effects of the bending modulus G_b become stronger for a higher mode number, which is associated with higher amplitude of bending of the coating.

The role of liquid viscosity is appreciable and cannot be ignored. The natural frequency ω_k of mode 2 decreases obviously with liquid viscosity μ_l. The variations of ω_k versus μ_l for higher

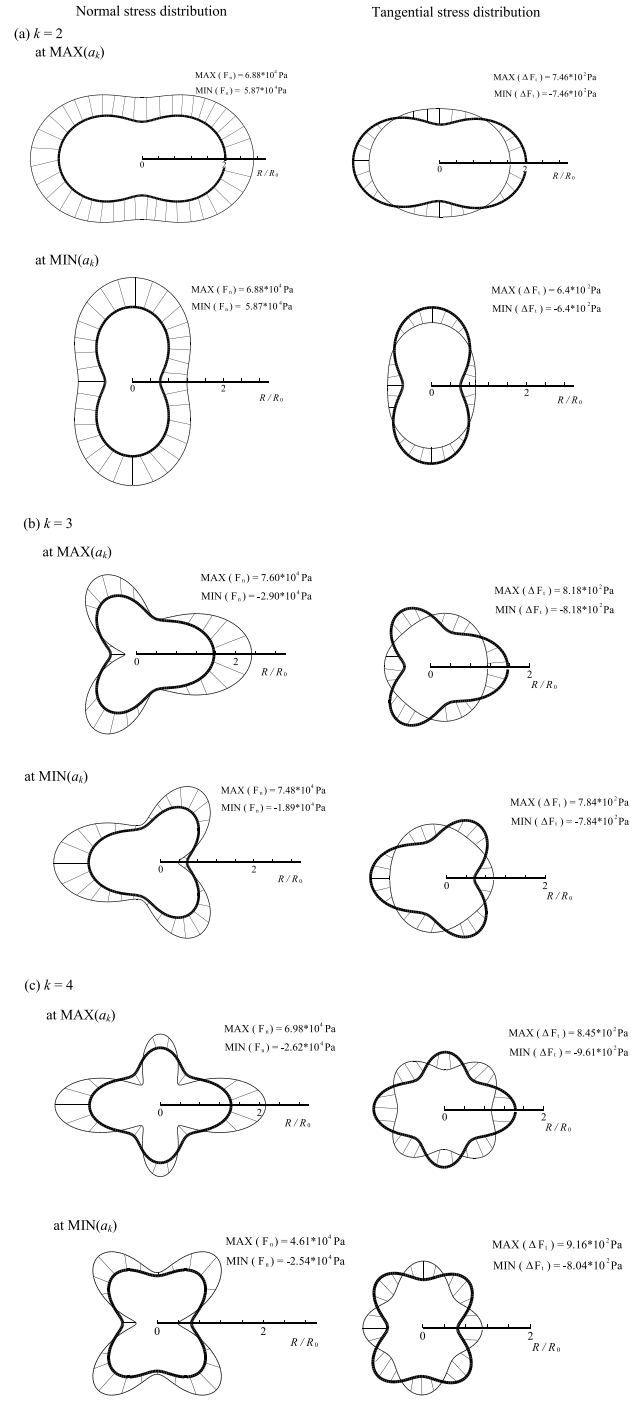

FIG. 5. Shapes of an EMB at maximal and minimal a_k, and distributions of normal and tangential stresses at shape modes for (a) $k = 2$, (b) $k = 3$, and (c) $k = 4$, respectively. The thick lines represent the bubble shape and the thin lines the distribution of stress. For normal stress (left column), the inward and outward lines embody the direction of stress. For tangential stress (right column), the inward lines represent compression and the outward lines represent extension.

shape modes $k = 3, 4$ are nonmonotonic, due to the complicated relationship (2.30) of the natural frequency in terms of the viscosities of liquid and membrane, and the dependency of the boundary layer thickness χ on the viscosity of liquid (2.14).

The natural frequencies obtained by the numerical results of the dynamic modelling (2.8) and (2.11)–(2.13) are also displayed for comparison and validation. The analytical results agree well

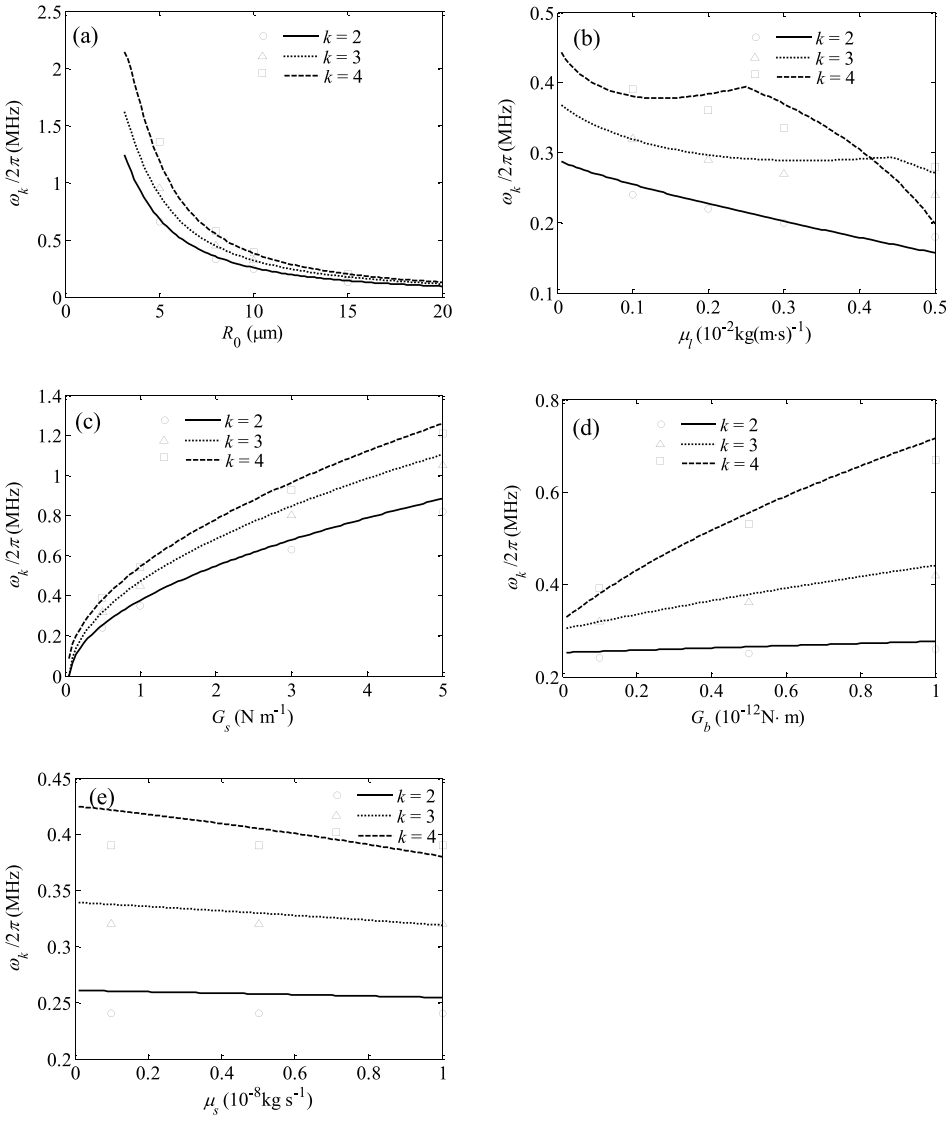

FIG. 6. Natural frequencies for shape modes $k = 2$, 3, 4 of an EMB versus (a) equilibrium radius R_0, (b) liquid viscosity μ_l, (c) elastic modulus G_s, (d) bending modulus G_b, and (e) membrane viscosity μ_s. The parameters are $R_0 = 10$ μm, $G_s = 0.5$ N m^{-1}, $G_b = 1\times10^{-13}$ N m, $\mu_s = 1\times10^{-8}$ kg s^{-1}, and $\mu_l = 1\times10^{-3}$ kg (m s)$^{-1}$. The results according to (2.30) are displayed in solid, dotted, and dashed lines for $k = 2$, 3, and 4, respectively. The numerical results based on (2.8) and (2.11)–(2.13) are displayed in symbols of circles, triangles, and squares for $k = 2$, 3, 4 respectively for validation.

with the numerical results for $\mu_l \le 1\times10^{-3}$ kg (m s)$^{-1}$ and the agreements stand for shape mode 2 at larger fluid viscosity (see Fig. 6(b)). The analytical solution predicts reasonably good results for shape modes 3, 4 for $\mu_l \le 3\times10^{-3}$ kg (m s)$^{-1}$, $\mu_l \le 1\times10^{-3}$ kg (m s)$^{-1}$, respectively. However, the discrepancy between them increases with the mode number and fluid viscosity, since high shape mode and non-small viscosity are associated with non-negligible nonlinear effects.

E. Toroidal component of vorticity

Only the toroidal component $T(r,t)$ contributes to the vorticity dissipation, due to axisymmetry, as commented in Sec. II A. In this section, we investigate the toroidal component of vorticity near the bubble surface to analyze viscous effects of liquid, by solving Equation (2.8) for $T(r,t)$. The liquid viscosity is selected as $\mu_l = 0.5\times10^{-3}$, 1×10^{-3}, and 0.5×10^{-2} kg (m s)$^{-1}$, respectively. The remaining parameters are the same as in Fig. 2 (for $\mu_l \neq 0$, $\mu_s \neq 0$).

A radial oscillation is considered for simplicity and illustration purpose,

$$R = R_0 (1 + \alpha \sin(\omega_d t)), \tag{3.1}$$

with the oscillatory amplitude $\alpha = 0.2$ and frequency $\omega_d = \omega_0$, where ω_0 is given by (2.10). The initial disturbance in shape mode is set as $a_k(0)/R_0 = 0.1$, and only the second order mode $k = 2$ is presented as an example.

Figure 7 shows the distributions of $T(r,t)$ along the normal direction $\eta = [r - R(t)]/R(t)$ on the bubble surface, at the times $0.2T_d$, $0.4T_d$, $0.6T_d$, $0.8T_d$, and $1.0T_d$ ($T_d = 2\pi/\omega_d$), respectively. For comparison, the results for a gas bubble with the same initial size are also displayed, where surface tension is set as $\gamma = 0.0729$ N m^{-1}. Figs. 7(a)-7(c) are for the results for an EMB, and Figs. 7(d)-7(f) are for the gas bubble.

The magnitudes of the toroidal component at the surfaces of both the gas bubble and encapsulated bubble decrease with viscosity. This is because that a large viscosity attenuates the shape disturbance, and thus restrains the production of vorticity. However, the dissipative length scale of vorticity increases with viscosity.

The magnitude of toroidal component at the surface of a gas bubble is much smaller than that of an EMB, although their boundary layer thicknesses are comparable. This explains the appreciable difference in the natural frequencies without and with viscous effects for an EMB, and the slight difference between them for a gas bubble. For a gas bubble, the vorticity produced by the shape deformation is relatively small due to the free-slip condition on the bubble interface. For this reason, dynamics of a gas bubble usually can be approximated by the inviscid flow theory. In contrast, the vorticity generation on a deformed encapsulated bubble cannot be neglected. That is why the viscosity of liquid plays an important role in the natural frequency of shape modes for an EMB.

We calculate the thickness of the viscous boundary layer using (2.14) for the cases in Fig. 7, with the results listed in Table III. Similar features as displayed in Fig. 7 are observed in the table: the thickness of the viscous boundary layer for a gas bubble is comparable with or slightly larger than that for an encapsulated bubble, and the thickness increases with the viscosity for both gas and encapsulated bubbles.

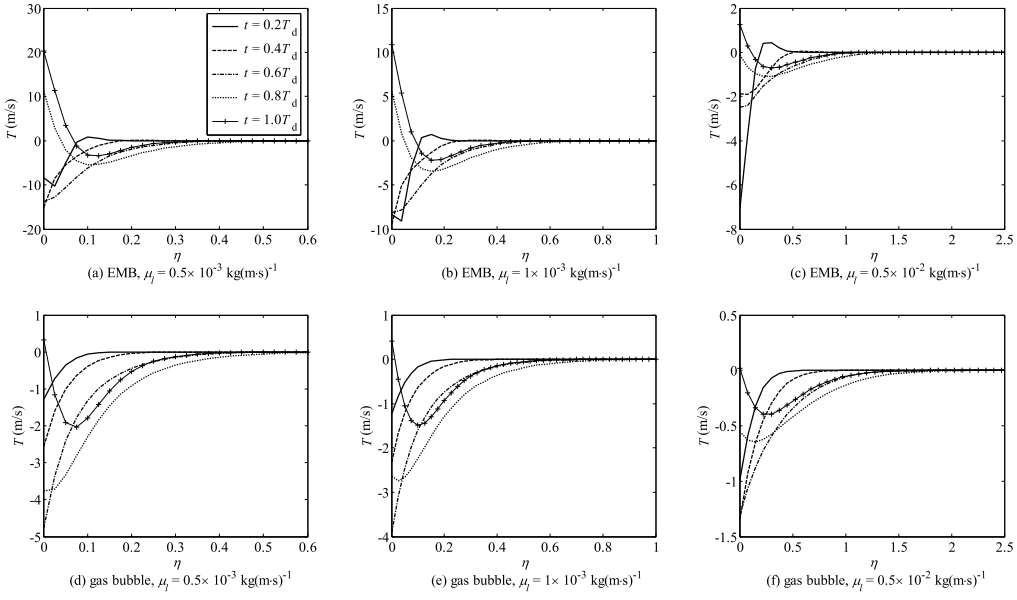

FIG. 7. Toroidal distribution of vorticity along the normal direction η of the surface of an EMB for (a)-(c) with $R_0 = 10$ μm, $G_s = 0.5$ N m^{-1}, $G_b = 1\times10^{-13}$ N m, $\mu_s = 1\times10^{-8}$ kg s^{-1} and a gas bubble (d)-(f) with $R_0 = 10$ μm, $\gamma = 0.0729$ N m^{-1}. The liquid viscosity is $\mu_l = 0.5\times10^{-3}$ kg (m s)$^{-1}$ for (a) and (d), 1×10^{-3} kg (m s)$^{-1}$ for (b) and (e), 0.5×10^{-2} kg (m s)$^{-1}$ for (c) and (f).

TABLE III. Thickness of boundary layer calculated by (2.14) for the cases in Fig. 7.

μ_l (kg (m s)$^{-1}$)	0.5×10^{-3}	1×10^{-3}	0.5×10^{-2}
χ/R_0 (EMB)	0.039	0.056	0.13
χ/R_0 (gas bubble)	0.048	0.068	0.15

IV. SUMMARY AND CONCLUSIONS

The dynamics of encapsulated microbubbles (EMBs) subject to ultrasound have wide and important applications in biomedicine. The nonspherical shape mode of an EMB is one of the core mechanisms of the applications and therefore its natural frequency is a fundamentally important parameter. Using linear stability analysis, we show that the shape oscillation is stable and damps with the viscosities of liquid and membrane, but oscillates at constant amplitude when both the viscosities are zero. We derive an explicit expression for the natural frequency of the shape modes for an EMB in a viscous Newtonian liquid as follows:

$$\begin{aligned}\omega_k^2 = {} & (k-1)(k+1)(k+2)\frac{\gamma}{\rho R_0^3} \\ & + 2(k-1)(k+1)(k+2)\frac{G_s}{\rho R_0^3}\frac{(2k^2+2k-3)(k^2+k-1+\upsilon)G_b+6G_sR_0^2}{(k^2+k-1+\upsilon)G_b+2(2k^2+2k-1)G_sR_0^2} \\ & - \left[(k+2)\left(\frac{kR_0}{2\chi}-k^2+1\right)\frac{\mu_l}{\rho R_0^2}-(k-1)(k+1)(k+2)\frac{\mu_s}{\rho R_0^3}\right. \\ & \left. + k(k+1)(k+2)\frac{\left((k^2+k-1+\upsilon)G_b+6G_sR_0^2\right)\left(R_0^2\mu_l+2(k^2-1)\chi\mu_s\right)}{2\rho R_0^3\chi\left((k^2+k-1+\upsilon)G_b+2(2k^2+2k-1)G_sR_0^2\right)}\right]^2,\end{aligned} \tag{2.30}$$

in terms of the shape mode k, the equilibrium radius of the bubble R_0, the density ρ and viscosity μ_l of liquid, surface tension γ, the elastic modulus G_s, bending modulus G_b, Poisson ratio υ, and viscosity μ_s of the coating. Here $\chi = \min\left(\sqrt{\frac{\mu_l}{\rho\omega_M}}, \frac{R_0}{2k}\right)$, $\omega_M = \max(\omega_d, \omega_0)$, $\omega_0 = \sqrt{\frac{3\Gamma p_\infty}{\rho R_0^2} + \frac{(6\Gamma-2)\gamma}{\rho R_0^3} + \frac{12G_s}{\rho R_0^3}}$, where Γ is the polytropic index of the bubble gas. The analytical expression is validated by comparing to the numerical results for an EMB oscillating in shape modes.

We have investigated the natural frequency of shape modes in terms of various parameters and observed the following features.

The natural frequency of shape modes shifts appreciably due to the viscosity of the liquid. The significant viscous effects are due to the no-slip condition for the liquid flow at the membrane interface and the vorticity retarding the flow near the surface.

The natural frequency increases with the mode number, and the elastic modulus and bending modulus of the membrane, but decreases with the equilibrium bubble radius and membrane viscosity. By comparison, the elastic modulus plays more important roles in the natural frequency for all modes and the bending modulus does for higher order modes.

Shape instability for an EMB is prone to appear if $2\omega_k/\omega_d = n$, where ω_k is the natural frequency of shape modes, ω_d is the driving frequency of the acoustic wave, and n is a natural number. The weak spots of the membrane of an EMB occur at its concave summits, where the tangential extension is maximal. The shift of the natural frequency due to viscous effects is thus critical in setting the applied frequency of ultrasound to avoid or activate the shape modes of EMBs, which should be considered in the applications of medical ultrasound.

ACKNOWLEDGMENTS

We thank Professors S. Takagi and K. Sugiyama for the valuable comments on the mathematical model for the dynamics of an EMB. This work was supported partially by the National Natural Science Foundation of China (Grant No. 11302128).

APPENDIX: THE DAMPING COEFFICIENT GIVEN IN (A1) IS NON-NEGATIVE

For clearness, we re-write Equation (2.27a) as follows:

$$\begin{aligned}\Psi \;=\; & 2(k+2)\left(\frac{kR_0}{2\chi}-k^2+1\right)\frac{\mu_l}{\rho R_0^2}-2(k-1)(k+1)(k+2)\frac{\mu_s}{\rho R_0^3}\\ & +\;k(k+1)(k+2)\frac{\left((k^2+k-1+\upsilon)G_b+6G_sR_0^2\right)\left(R_0^2\mu_l+2(k^2-1)\chi\mu_s\right)}{\rho R_0^3\chi\left((k^2+k-1+\upsilon)G_b+2(2k^2+2k-1)G_sR_0^2\right)}.\end{aligned} \tag{A1}$$

The first and third terms are positive, and the second term is negative. To show that Ψ is non-negative, it will be sufficient to show that the magnitude of the second term in (A1) is equal or smaller than the third term.

As $k \geq 2$ and all the other parameters occurred are non-negative, we have

$$(k^2+k-1+\upsilon)G_b < k(k+1)(k^2+k-1+\upsilon)G_b, \tag{A2}$$

$$2(2k^2+2k-1)G_sR_0^2 < 6k(k+1)G_sR_0^2. \tag{A3}$$

Adding the above two inequalities yields

$$(k^2+k-1+\upsilon)G_b+2(2k^2+2k-1)G_sR_0^2 < k(k+1)\left((k^2+k-1+\upsilon)G_b+6G_sR_0^2\right). \tag{A4}$$

Using (A4), one can obtain

$$\begin{aligned}&2(k-1)\mu_s\chi\left((k^2+k-1+\upsilon)G_b+2(2k^2+2k-1)G_sR_0^2\right)\\ &< k\left((k^2+k-1+\upsilon)G_b+6G_sR_0^2\right)\left(R_0^2\mu_l+2(k^2-1)\chi\mu_s\right).\end{aligned} \tag{A5}$$

This can be arranged as

$$2(k-1)\mu_s \leq k\frac{\left((k^2+k-1+\upsilon)G_b+6G_sR_0^2\right)\left(R_0^2\mu_l+2(k^2-1)\chi\mu_s\right)}{\chi\left((k^2+k-1+\upsilon)G_b+2(2k^2+2k-1)G_sR_0^2\right)}. \tag{A6}$$

The equal only satisfies when $\mu_s = 0$. From (A6), we know that the magnitude of the second term in (A1) is equal or smaller than the third term.

[1] R. Gramiak and P. M. Shah, "Echocardiography of the aortic root," Invest. Radiol. **3**, 356–366 (1968).
[2] K. Ferrara, R. Pollard, and M. Borden, "Ultrasound microbubble contrast agents: Fundamentals and application to gene and drug delivery," Annu. Rev. Biomed. Eng. **9**, 415–472 (2007).
[3] S. Dindyal and C. Kyriakides, "Ultrasound microbubble contrast and current clinical applications," Recent Pat. Cardiovasc. Drug Discovery **6**, 27–41 (2011).
[4] N. A. Hosny, G. Mohamedi, P. Rademeyer, J. Owen, Y. Wu, M. X. Tang, R. J. Eckersley, E. Stride, and M. K. Kuimova, "Mapping microbubble viscosity using fluorescence lifetime imaging of molecular rotors," Proc. Natl. Acad. Sci. **110**, 9225–9230 (2013).
[5] C. C. Coussios and R. A. Roy, "Applications of acoustics and cavitation to noninvasive therapy and drug delivery," Annu. Rev. Fluid Mech. **40**, 395–420 (2008).
[6] B. Dollet, S. M. van der Meer, V. Garbin, N. de Jong, D. Lohse, and M. Versluis, "Nonspherical oscillations of ultrasound contrast agent microbubbles," Ultrasound Med. Biol. **34**, 1465–1473 (2008).
[7] Q. X. Wang and K. Manmi, "Microbubble dynamics near a wall subjected to a travelling acoustic wave," Phys. Fluids **26**, 032104 (2014).
[8] Q. X. Wang and K. Manmi, "Numerical modelling of the 3D dynamics of ultrasound contrast agent microbubbles using the BIM," Phys. Fluids **27**, 022104 (2015).
[9] J. L. Foley, S. Vaezy, and L. A. Crum, "Applications of high-intensity focused ultrasound in medicine: Spotlight on neurological applications," Appl. Acoust. **68**, 245–259 (2007).
[10] S. Martynov, E. Stride, and N. Saffari, "The natural frequencies of microbubble oscillation in elastic vessels," J. Acoust. Soc. Am. **126**, 2963–2972 (2009).
[11] E. P. Stride and C. C. Coussios, "Cavitation and contrast: The use of bubbles in ultrasound imaging and therapy," Proc. Inst. Mech. Eng., Part H **224**, 171–191 (2010).
[12] W. Kreider, L. A. Crum, M. R. Bailey, and O. A. Sapozhnikov, "A reduced-order, single-bubble cavitation model with applications to therapeutic ultrasound," J. Acoust. Soc. Am. **130**, 3511–3530 (2011).
[13] S. Ibsen, M. Benchimol, D. Simberg, and S. Esener, "Ultrasound mediated localized drug delivery," Adv. Exp. Med. Biol. **733**, 145–153 (2012).
[14] H. Chen and J. Hwang, "Ultrasound-targeted microbubble destruction for chemotherapeutic drug delivery to solid tumors," J. Ther. Ultrasound **1**, 10 (2013).
[15] G. A. Curtiss, D. M. Leppinen, Q. X. Wang, and J. R. Blake, "Ultrasonic cavitation near a tissue layer," J. Fluid Mech. **730**, 245–272 (2013).

[16] Q. X. Wang and J. R. Blake, "Non-spherical bubble dynamics in a compressible liquid. Part 1. Travelling acoustic wave," J. Fluid Mech. **659**, 191–224 (2010).
[17] Q. X. Wang and J. R. Blake, "Non-spherical bubble dynamics in a compressible liquid. Part 2. Standing acoustic wave," J. Fluid Mech. **679**, 559–581 (2011).
[18] Q. X. Wang, K. Manmi, and K. K. Liu, "Cell mechanics in biomedical cavitation," J. R. Soc. Interface Focus **5**(5), 20150018 (2015).
[19] W. L. Nyborg, "Ultrasonic microstreaming and related phenomena," Br. J. Cancer, Suppl. **45**, 156–160 (1982).
[20] A. A. Doinikov and A. Bouakaz, "Effect of a distant rigid wall on microstreaming generated by an acoustically driven gas bubble," J. Fluid Mech. **742**, 425–445 (2014).
[21] H. Lamb, *Hydrodynamics* (Cambridge University Press, 1932).
[22] A. Prosperetti, "Viscous effects on perturbed spherical flows," Q. Appl. Math. **34**(4), 339–352 (1977).
[23] H. Takahira, T. Akamatsu, and S. Fujikawa, "Dynamics of two nonspherical bubbles in a viscous liquid," Trans. JSME B **57**, 447–455 (1991).
[24] S. Hilgenfeldt, D. Lohse, and M. P. Brenner, "Phase diagrams for sonoluminescing bubbles," Phys. Fluids **8**(11), 2808–2826 (1996).
[25] Y. Hao and A. Prosperetti, "The effect of viscosity on the spherical stability of oscillating gas bubbles," Phys. Fluids **11**, 1309–1317 (1999).
[26] S. Shaw, "The stability of a bubble in a weakly viscous liquid subject to an acoustic traveling wave," Phys. Fluids **21**(2), 022104 (2009).
[27] R. Gaudron, M. T. Warnez, and E. Johnsen, "Bubble dynamics in a viscoelastic medium with nonlinear elasticity," J. Fluid Mech. **766**, 54–75 (2015).
[28] M. Lankford, C. Z. Behm, J. Yeh, A. L. Klibanov, P. Robinson, and J. R. Lindner, "Effect of microbubble ligation to cells on ultrasound signal enhancement: Implications for targeted imaging," Invest. Radiol. **41**, 721 (2006).
[29] V. Garbin, D. Cojoc, E. Ferrari, E. Di Fabrizio, M. L. J. Overvelde, S. M. van der Meer, N. de Jong, D. Lohse, and M. Versluis, "Changes in microbubble dynamics near a boundary revealed by combined optical micromanipulation and high-speed imaging," Appl. Phys. Lett. **90**, 114103 (2007).
[30] M. Overvelde, V. Garbin, B. Dollet, N. de Jong, D. Lohse, and M. Versluis, "Dynamics of coated microbubbles adherent to a wall," Ultrasound Med. Biol. **37**, 1500–1508 (2011).
[31] K. Tsiglifis and N. A. Pelekasis, "Parametric stability and dynamic buckling of an encapsulated microbubble subject to acoustic disturbances," Phys. Fluids **23**, 012102 (2011).
[32] Y. Liu, K. Sugiyama, S. Takagi, and Y. Matusmoto, "Surface instability of an encapsulated bubble induced by an ultrasonic pressure wave," J. Fluid Mech. **691**, 315–340 (2012).
[33] D. B. Khismatullin, "Resonance frequency of microbubbles: Effect of viscosity," J. Acoust. Soc. Am. **116**, 1463–1473 (2004).
[34] C. M. Bender and S. A. Orszag, *Advanced Mathematical Methods for Scientists and Engineers* (McGraw-Hill, 1978).
[35] Q. X. Wang, "Underwater explosion bubble dynamics in a compressible liquid," Phys. Fluids **25**, 072104 (2013).
[36] Q. X. Wang, "Multi-oscillations of a bubble in a compressible liquid near a rigid boundary," J. Fluid Mech. **745**, 509–536 (2014).
[37] J. Loughran, R. J. Eckersley, and M. X. Tang, "Modeling non-spherical oscillations and stability of acoustically driven shelled microbubbles," J. Acoust. Soc. Am. **131**(6), 4349–4357 (2012).
[38] J. R. Lindner, "Microbubbles in medical imaging: Current applications and future directions," Nat. Rev. Drug Discovery **3**, 527–532 (2004).
[39] D. Barthès-Biesel, "Motion of a spherical microcapsule freely suspended in a linear shear flow," J. Fluid Mech. **100**, 931–953 (1980).
[40] D. Barthès-Biesel and J. M. Rallison, "The time-dependent deformation of a capsule freely suspended in a linear shear flow," J. Fluid Mech. **113**, 251–267 (1981).
[41] D. Barthès-Biesel and H. Sgaier, "Role of membrane viscosity in the orientation and deformation of a spherical capsule suspended in shear flow," J. Fluid Mech. **160**, 119–135 (1985).
[42] A. Diaz, N. Pelekasis, and D. Barthès-Biesel, "Transient response of a capsule subjected to varying flow conditions: Effect of internal fluid viscosity and membrane elasticity," Phys. Fluids **12**, 948–957 (2000).
[43] C. Pozrikidis, "The axisymmetric deformation of a red blood cell in uniaxial straining stokes flow," J. Fluid Mech. **440**, 231–254 (1990).
[44] S. Ramanujan and C. Pozrikidis, "Deformation of liquid capsules enclosed by elastic membranes in simple shear flow: Large deformations and the effect of fluid viscosities," J. Fluid Mech. **361**, 117–143 (1998).
[45] S. Takagi, T. Yamada, X. Gong, and Y. Matsumoto, "The deformation of a vesicle in a linear shear flow," J. Appl. Mech. **76**, 021207 (2009).
[46] Y. Liu, K. Sugiyama, S. Takagi, and Y. Matusmoto, "Numerical study on the shape oscillation of an encapsulated microbubble in ultrasound field," Phys. Fluids **23**, 041904 (2011).
[47] A. E. Green and J. E. Adkins, *Large Elstic Deformations and Non-Linear Continuum Mechanics* (Clarendon Press Oxford, 1960).
[48] M. Mooney, "A theory of large elastic deformation," J. Appl. Phys. **11**, 582–592 (1940).
[49] A. E. H. Love, "The small free vibrations and deformation of a thin elastic shell," Philos. Trans. R. Soc., A **179**, 491–546 (1888).
[50] S. M. van der Meer, B. Dollet, M. M. Voormolen, C. T. Chin, A. Bouakaz, N. de Jong, M. Versluis, and D. Lohse, "Microbubble spectroscopy of ultrasound contrast agents," J. Acoust. Soc. Am. **118**, 3499–3505 (2007).
[51] M. Versluis, D. E. Goertz, P. Palanchon, I. L. Heitman, S. M. van der Meer, B. Dollet, N. de Jong, and D. Lohse, "Microbubble shape oscillations excited through ultrasonic parametric driving," Phys. Rev. E **82**, 026321 (2010).
[52] S. Shaw, "Translation and oscillation of a bubble under axisymmetric deformation," Phys. Fluid **18**(7), 072104 (2006).

[53] L. G. Leal, *Advanced Transport Phenomena: Fluid Mechanics and Convective Transport Processes* (Cambridge University Press, 2007).
[54] M. S. Plesset, "On the stability of fluid flows with spherical symmetry," J. Appl. Phys. **25**, 96–98 (1954).
[55] T. S. Lundgren and N. N. Mansour, "Vortex ring bubbles," J. Fluid Mech. **72**, 391–399 (1991).
[56] S. Hilgenfeldt, D. Lohse, and M. Brenner, "Phase diagrams for sonoluminescing bubbles," Phys. Fluids **21**, 2808–2826 (1996).
[57] Y. C. Fung, *Blood Rheology in Microvessels. Biomechanics–Mechanical Properties of Living Tissues* (Science Technique Publisher, China, 1986).
[58] S. B. Feinstein, R. M. Lang, C. Dick, A. Neumann, J. Al-Sadir, K. G. Chua, J. Carroll, T. Feldman, and K. M. Borow, "Contrast echocardiography during coronary arteriography in humans: Perfusion and anatomic studies," J. Am. Coll. Cardiol. **11**, 59–65 (1998).
[59] L. Hoff, P. C. Sontum, and J. M. Hovem, "Oscillations of polymeric microbubbles: Effect of the encapsulating shell," J. Acoust. Soc. Am. **107**, 2272–2280 (2000).
[60] N. de Jong and L. Hoff, "Ultrasound scattering properties of albunex microspheres," Ultrasonics **31**, 175–181 (1993).
[61] N. C. Nanda, "Echo enhancers—How safe are they?," in *Advances in Echo Imaging using Contrast Enhancement*, edited by N. C. Nanda and R. Sclief (Kluwer, Dordrecht, 1993), pp. 97–110.
[62] E. C. Unger, T. Porterc, W. Culpd, R. Labella, T. Matsunaga, and R. Zutshi, "Therapeutic applications of lipid-coated microbubbles," Adv. Drug Delivery Rev. **56**, 1291–1314 (2004).
[63] K. Bjerknes, P. C. Sontum, G. Smistad, and I. Agerkvista, "Preparation of polymeric microbubbles: Formulation studies and product characterisation," Int. J. Pharm. **158**, 129–136 (1997).
[64] D. A. Fedosov, W. Pan, B. Caswell, G. Gompper, and G. E. Karniadakis, "Predicting human blood viscosity in silico," Proc. Natl. Acad. Sci. **108**, 11772–11777 (2011).
[65] S. Unnikrishnan and A. L. Klibanov, "Microbubbles as ultrasound contrast agents for molecular imaging: Preparation and application," Am. J. Roentgenol. **199**, 292–299 (2012).
[66] C. Pozrikidis, "Effect of membrane bending stiffness on the deformation of capsules in simple shear flow," J. Fluid Mech. **440**, 269–291 (2001).
[67] M. Postema, A. van Wamel, C. T. Lancee, and N. de Jong, "Ultrasound-induced encapsulated microbubble phenomena," Ultrasound Med. Biol. **30**, 827–840 (2004).